

Magnetic and nematic order of Bose-Fermi mixtures in moiré superlattices of 2D semiconductors

Feng-Ren Fan,^{1,2,*} Tixuan Tan,^{2,3,*} Chengxin Xiao,^{1,2} and Wang Yao^{1,2,†}

¹*New Cornerstone Science Laboratory, Department of Physics,
The University of Hong Kong, Hong Kong, China*

²*HK Institute of Quantum Science and Technology, University of Hong Kong, Hong Kong, China*

³*Department of Physics, Stanford University, Stanford, CA 94305, USA*

We investigate the magnetic orders in a mixture of a boson (exciton) and a fermion (electron or hole) trapped in transition-metal dichalcogenides moiré superlattices. A sizable antiferromagnetic exchange interaction is found between a carrier and an interlayer exciton trapped at different high symmetry points of the moiré supercell. This interaction at a distance much shorter than the carrier-carrier separation dominates the magnetic order in the Bose-Fermi mixture, where the carrier sublattice develops ferromagnetism opposite to that in the exciton sublattice. We demonstrate the possibility of increasing the Curie temperature of moiré carriers through electrical tuning of the exciton density in the ground state. In a trilayer moiré system with a p-n-p type band alignment, the exciton-carrier interplay can establish a layered antiferromagnetism for holes confined in the two outer layers. We further reveal a spontaneous nematic order in the Bose-Fermi mixture, arising from the interference between the Coulomb interaction and p-wave interlayer tunneling dictated by the stacking registry.

Introduction. Moiré superlattices in the twisted layered structures of 2D crystals have sparked tremendous interest as highly tunable physical platforms that can host exotic correlated states of matter [1–8]. In particular, transition metal dichalcogenides (TMD) as a semiconducting building block have enabled the exploration of both fermionic (electronic) and bosonic (excitonic) many-body phenomena on a common moiré platform [6, 7, 9]. The moiré of twisted TMDs forms superlattice confinement for electron and hole, as well as for exciton as their bound state [10–15]. At a heterointerface where hole energetically favors one layer while electron favors the other, excitons have an interlayer configuration which endows them an ultralong lifetime and a permanent electrical dipole [16]. These bosonic composite particles can be injected either optically, or electrically through electron hole co-doping [17]. The strong dipole-dipole interaction between excitons trapped in the moiré lattice has enabled a playground for studying Bose-Hubbard type physics [18–21]. Moreover, with optical control of exciton doping and gate control of carrier doping, recent experiments have realized Bose-Fermi mixtures for the exploration of their interplay in WS₂/WSe₂ heterobilayers [22–24].

Magnetic interactions and magnetic orders are of paramount interest in the context of various TMDs moiré superlattices [22, 25, 26]. The discovery of intrinsic ferromagnetism in twisted bilayer MoTe₂ [26] has heralded the experimental observations of integer and fractional quantum anomalous Hall effects in this exciting platform [27–30]. Curie temperature sets a limit for the exploration of these exotic topological states of matter relying on broken time reversal symmetry. The existing observations

in moiré platforms are reported in the order of 1 – 10 K [27–32], likely limited by the density of the moiré carriers. Numerical studies suggest that the magnon gap decreases with lower carrier concentration, indicating the decreased stability of fractional quantum anomalous Hall phases at smaller filling fraction [33]. This prompts the question of how to increase the stability of the magnetic order and the critical temperatures of the phenomena for easier experimental access, especially at low carrier filling fractions. Notably, experiments have discovered that, in the dilute filling limit of a WS₂/WSe₂ moiré, light irradiation can help to establish ferromagnetic order [22], where the role of optically injected mobile interlayer excitons has been identified as mediating a long-range RKKY type of magnetic interaction [34].

In this paper, we investigate the magnetic orders in the Bose-Fermi mixture of carriers and excitons both trapped in the moiré superlattices of TMDs heterostructures, with exciton density electrically tuned at fixed carrier filling. Wave-packet model analysis and self-consistent Hartree-Fock mean-field calculations both find that the exchange interaction between a carrier and an interlayer exciton in the moiré traps leads to a sizable magnetic interaction, which, counterintuitively, are aligned in an antiparallel-spin configuration. When carriers and excitons are trapped at different high symmetry points of the moiré supercell, their nearest neighbor interactions at a distance much shorter than the carrier-carrier separation establish a joint magnetic order in the Bose-Fermi mixture, where the carrier sublattice develops robust ferromagnetic order opposite to that in the exciton sublattice. The possibility of increasing the Curie temperature of moiré carriers is demonstrated through electrical tuning of the exciton density in the ground state. In a trilayer moiré system with a p-n-p type band alignment, we show that the exciton-carrier interplay can establish a layered antiferromagnetism for holes confined in the two outer

* These two authors contributed equally

† wangyao@hku.hk

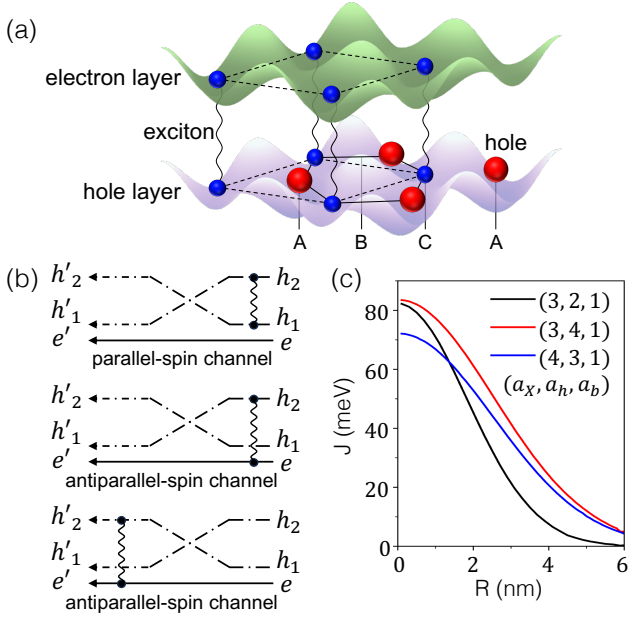


FIG. 1. (Color online) (a) Schematic illustration of mixed Boson-Fermion (exciton-hole) mixtures in heterobilayer moiré superlattice, where A, B, and C are the three high-symmetry points in the moiré unit cell. The green and purple curved surfaces represent the moiré potential surfaces of the conduction and valence bands, respectively. The color of the balls corresponds respectively to their spin. (b) Feynman diagrams of the three exciton-hole (eh_1-h_2) exchange channels. The solid lines denote electrons, and the dotted lines denote holes. The top channel favors parallel-spin alignment, while the bottom two channels favor antiparallel-spin alignment. (c) Exciton-carrier exchange J as a function of their distance, where a_x, a_e , and a_b are the Bohr radius of the exciton-wave packet, hole-wave packet, and exciton, respectively (Appendix B). The positive J value means the antiparallel-spin exchange dominates. R is the distance between exciton and hole wave packet.

layers. We further reveal a spontaneous nematic order in the Bose-Fermi mixture, arising from the interference between interlayer tunneling that creates electron-hole pair in p-wave channel and Coulomb interaction that favors s-wave channel instead.

Exciton-carrier exchange. Consider a type-II heterointerface at carrier filling $\nu = -1$, i.e. one hole per moiré unit cell (MUC). Fig. 1(a) shows a moiré landscape in which the doped holes (red spheres) and interlayer excitons (pairs of blue spheres) are trapped at different high-symmetry points in the MUC, denoted as A and C sites. As we will show by Hartree-Fock calculation, this is an energetically favorable configuration when holes and electrons have their energy minima at A and C sites respectively, like in the H-stacking WSe_2/WS_2 bilayer [23, 35], and when all A sites are occupied by a doped hole. In such configuration, the exciton-carrier distance is much shorter compared with the carrier-carrier distance. The

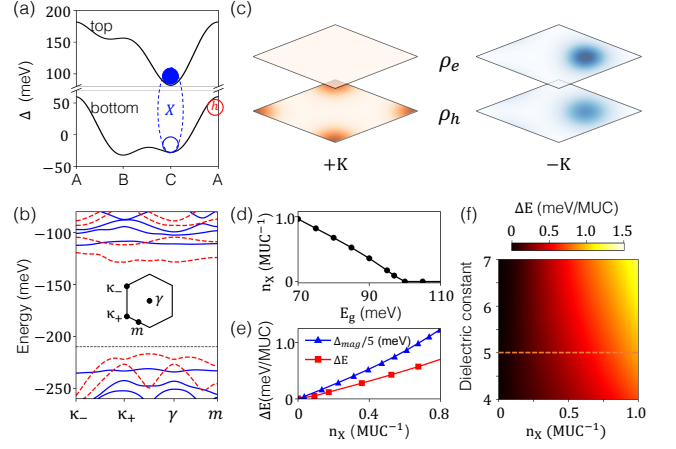


FIG. 2. (Color online) (a) Moiré potentials of top and bottom layers along the long diagonal of the moiré unit cell [Fig. 1(a)]. (b) Hartree-Fock band of heterobilayer moiré superlattice at filling $\nu = -1$. Dashed red (solid blue) lines are the bands associated with $K(-K)$ valley. The black dashed line denote the Fermi level. Parameters used are $m_t = 0.45 m_e$, $m_b = -0.25 m_e$, $V_t/b = 10$ meV, $\phi_t/b = 45/-3^\circ$, $\epsilon_r = 5$, $w = 0$, $E_g = 75$ meV. (c) Layer resolved charge distribution of the ground state. All the doped holes (left panel) are spin up, locked with valley $+K$. (d) Variation of exciton density as a function of energy gap. (e) Variations of energy difference ($\Delta E \equiv E_{AFM} - E_{FM}$) and magnon gap (Δ_{mag}) as functions of exciton density (details in Appendix A). (f) Phase diagram of ΔE as a function of exciton density and relative dielectric constant. Dashed line indicates the cut shown in subfigure (d).

Coulomb exchange interaction between the carrier and exciton therefore becomes the dominant magnetic interaction that determines the ground state of the mixture.

This Bose-Fermi mixtures can be described by a Heisenberg model with exchange energy J (Appendix B). There are three exciton-hole exchange channels associated with this process, as illustrated in Fig. 1(b): one channel (top panel) contributes parallel-spin exchange, while the bottom two contribute antiparallel-spin exchanges. The total exchange energy J is determined by the competition among these three channels.

We have calculated the total J values for ballpark realistic parameters, including the exciton Bohr radius a_b , exciton wave-packet radius a_x , carrier wave-packet radius a_h , and exciton-carrier separation R . This calculation assumes that the exciton center-of-mass wavefunction and carrier wavefunction are wave packets trapped by moiré potential (see details in Appendix B). As shown in Fig. 1(c), J is positive for a wide range of parameters, indicating an overall tendency toward antiparallel-spin alignment between excitons and carriers.

It has been established in a previous study [36] that a carrier doped heterobilayer moiré superlattice can be described by Hubbard model, and with one hole MUC the system hosts weak in-plane anti-ferromagnetic (AFM) or-

der among carriers. We show here, supported by the analytic argument given above and more numerical evidence below, that a ferromagnetic (FM) order among carriers can be established with the aid of exciton.

Exciton mediated FM order in heterobilayer moiré.

We first perform self-consistent Hartree-Fock (HF) calculations for heterobilayer moiré in the plane-wave basis to locate its ground state configurations. The single-particle Hamiltonian (with its time-reversal copy) is

$$H_{\uparrow} = \begin{pmatrix} \frac{(k-\kappa_-)^2}{2m_t} + V_t(\mathbf{r}) + E_g & T(\mathbf{r}) \\ T^\dagger(\mathbf{r}) & \frac{(k-\kappa_+)^2}{2m_b} + V_b(\mathbf{r}) \end{pmatrix}, \quad (1)$$

where $V_{t/b}(\mathbf{r}) = \sum_{i=1,3,5} 2V_{t/b} \cos(\mathbf{g}_i \cdot \mathbf{r} + \phi_{t/b})$ and $T(\mathbf{r}) = w(1 + \omega e^{i\mathbf{g}_2 \cdot \mathbf{r}} + \omega^2 e^{i\mathbf{g}_3 \cdot \mathbf{r}})$, with $\mathbf{g}_i = b_M [\cos \frac{(i-1)\pi}{3}, \sin \frac{(i-1)\pi}{3}]$, b_M is the moiré reciprocal lattice constant, $\omega = e^{i\frac{2n\pi}{3}}$, in which n is determined by angular momentum difference between orbitals involved. The moiré potential employed in the calculations for the heterobilayer system is ballpark realistic with $|V_{b/t}| = 10$ meV and their profile is a typical one capturing the feature that holes and electrons have their energy minima at different high symmetry points in an MUC, as shown in Fig. 2(a). We take moiré period 10 nm, and TMD lattice constant $a_0 = 0.347$ nm throughout this paper.

We focus on the scenario with filling factor $\nu = -1$, i.e., one hole per MUC. In the calculation, the type-II band gap E_g is taken to be slightly smaller compared to the interlayer exciton binding energy, so that Coulomb interaction leads to the spontaneous formation of excitons. The real-space charge density of ground state is shown in Fig. 2(c) and the corresponding band structure in Fig. 2(b). The doped hole is trapped in the bottom layer (valence band) around A point, while the interlayer exciton is trapped around C point, corresponding to the scenario of Fig. 1(a). In addition, they have opposite spin/valley quantum number. Thus, we observe a scenario in which the spontaneously formed exciton and doped carriers exhibit antiparallel-spin alignment.

We proceed to investigate the tunability and robustness of the observed magnetic ground state. In experiments, the exciton density may be tuned by the light intensity in the optically injected scenario [22], and by electrostatic gating in the co-doping scenario [17]. In the HF calculation, the density of the exciton is practically controlled by the band gap E_g that is tunable by the out-of-plane electric field. As E_g is decreased, the exciton density grows. The phase indicator ΔE is defined as the energy difference between two magnetic configurations (Appendix A): (1) FM state with all carriers being spin up locked with valley $+K$, (2) AFM state with half of the carriers spin up, while the other half spin down, i.e., $\Delta E \equiv E_{AFM} - E_{FM}$. We expand the system to 1×2 MUCs when performing the HF calculation, and the details are laid out in Appendix A.

As shown in Fig. 2(d), when E_g is tuned lower than a critical point, exciton spontaneously condenses (black

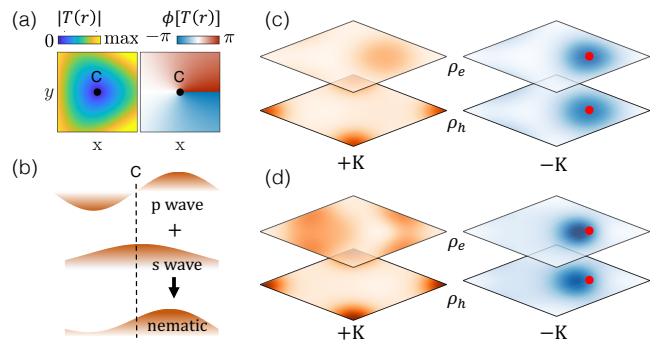


FIG. 3. (Color online) (a) Schematic illustration of the p-wave tunneling in real space. The left (right) panel is the tunneling magnitude (phase). (b) Schematic illustration of nematic order induced by s-p interference, where the dashed line denotes the rotation axis (high symmetry point). (c, d) Layer resolved charge distribution of $+K$ (upper panel) and $-K$ (lower panel) valley. The red points denote the high-symmetry point C. In (c), the interlayer tunneling $T(\mathbf{r})$ has an s-wave form in the vicinity of C point. While in (d), a different choice of ω leads to an interlayer tunneling $T(\mathbf{r})$ that has p-wave form in the vicinity of C point. As evident from the density profile, the C_3 symmetry is broken, nematic order emerges. The parameters used are the same as in Fig. 2 except $w = 3$ meV.

line), the system transforms to an exciton insulating state, and as shown in Fig. 2(e), ΔE (red line) deviates from zero concurrently with increasing exciton density. This indicates that the emergence of excitons facilitates the establishment of a magnetic order, specifically ferromagnetism, within the carrier sublattice. The full phase diagram is shown in Fig. 2(f) with various choices of exciton density n_X and dielectric constant ϵ_r . A positive phase indicator ΔE always occurs together with a non-zero exciton density n_X , and their magnitude is positively correlated, showing a robust exciton-mediated magnetic order in the heterobilayer moiré system.

We further carry out exact diagonalization on top of the self-consistent ground state, and calculate the magnon gap Δ_{mag} associated with flipping one hole's spin/valley (Appendix A). A non-zero magnon gap occurs simultaneously with the non-zero exciton density, as shown by blue-dot line Fig. 2(e). Both the ΔE and Δ_{mag} are positively correlated with n_X , so the injected exciton can help to stabilize the FM order among the doped carriers. This may be exploited for exploring correlation phenomena that rely on the ferromagnetic order of moiré carriers.

Nematic order in heterobilayer moiré. We then focus on the interplay between the Coulomb interaction and interlayer tunneling, both of which can lead to the formation of interlayer electron-hole pair. Coulomb interaction leads to exciton condensation in the s-wave channel, with a spontaneously determined global phase. On the other hand, the interlayer tunneling in the vicinity

of the high-symmetry stackings can have a p-wave symmetry [37]. The C_3 rotational symmetry dictates that interlayer tunneling coefficient $T(\mathbf{r})$ must have p-wave symmetry in the vicinity of two out of the three high symmetry points of the MUC [c.f. Fig. 3(a)] [38], whereas at the remaining site, $T(\mathbf{r})$ has the s-wave form. If exciton is formed at p-wave sites, the p-wave interlayer tunneling leads to electron-hole pair formation in the p-wave channel with a fixed global phase, and its interference with the Coulomb induced pairing in s-wave channel can shift the exciton wavefunction away from the high symmetry point, thereby break the C_3 rotation symmetry and introducing into nematic order [37]. This is schematically illustrated in Fig. 3(b).

Motivated by these considerations, we carry out HF calculation in the same heterobilayer system as in last section, with the interlayer tunneling $T(\mathbf{r})$ turned on. The resulting real-space density profile is shown in Fig. 3(c, d). In Fig. 3(c), $T(\mathbf{r})$ takes a form that has s-wave form in the vicinity of C site. As Coulomb interaction and interlayer tunneling both favor electron-hole pairing in the s-wave channel, the C_3 rotational symmetry is retained in the ground state. For the calculation in Fig. 3 (d), a different choice of parameter ω leads to a $T(\mathbf{r})$ that has p-wave form in the vicinity of C site. Compared with the density profile presented in Fig. 2(b) (where interlayer tunneling is switched off) and Fig. 3(c), apparent deviation of the center of exciton from the high-symmetry C point is observed. We also remark that in the pure-Coulomb case presented in Fig. 2(b) (without interlayer tunneling), the spontaneously formed exciton is fully polarized in one valley. However, as we turn on the tunneling, the exciton is not fully polarized as interlayer tunneling occurs in both valleys, as shown in Fig. 3 (c, d). Nevertheless, the ground state still prefers partial polarization where most excitons are in the opposite valley to the doped holes.

Layered AFM order in trilayer moiré. An immediate extension of the results established above is to multi-layer system. Consider a sandwich-like trilayer moiré heterostructure, as shown in Fig. 4(a), with the top and bottom layer (middle layer) hosting valence (conduction) band. If doped with holes, these carriers will be located in the top and bottom layers, and there is no magnetic interaction between them owing to the lack of spatial overlap.

The moiré potentials here depend on the relative interlayer translation [Fig. 4(a)] and orientation between layers [39]. A different configuration may yield different results, but the underlying physics remains the same. For simplicity, we focus on the scenario where the interlayer excitons from two interfaces are trapped in the same horizontal location [Fig. 4(b)]. In this configuration, two exciton holes (hollow circles) are well separated into the two outer layers, while the two exciton electrons (solid circles) exhibit a strong overlap in the middle layer. Because of the strong overlap between the two electrons in the middle layer, the Pauli exclusion forces these two excitons

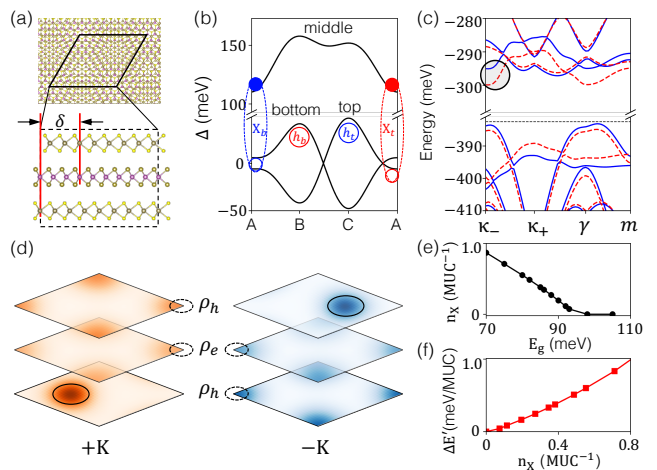


FIG. 4. (Color online) (a) Schematic illustration of sandwich-like trilayer moiré superlattice. The upper (lower) panel is the top (side) view, δ is the relative displacement between the top and bottom layers. (b) Moiré potentials of the sandwich-like moiré superlattice along the long diagonal of the moiré unit cell. (c) Hartree-Fock quasiparticle bands of the two-hole doped trilayer moiré superlattice, the black circle marks the two hole bands. Parameters used are $m_{t/b} = -0.25 m_e$, $m_m = 0.33 m_e$, $V_{t/b} = 8.6$ meV, $V_m = 5.0$ meV, $\phi_{t/m/b} = -96/173/84^\circ$ [39], $E_g = 75$ meV, $\epsilon_r = 5$. (d) Layer resolved charge distribution of $+K$ (left) and $-K$ (right) valley, in which the solid (dashed) circles denote the carrier holes (excitons). (e-f) Variation of (e) exciton density and (f) energy difference between the layered FM and AFM states as a function of energy gap and exciton density, respectively.

to be spin-antiparallel aligned [40]. With the exciton-carrier antiparallel-spin exchange interactions in the top and bottom layers, even when separated by a large distance, a layered AFM order can be established between the carriers trapped in the top and bottom layers.

This is verified by HF calculation in trilayer moiré with ballpark realistic parameters at filling factor $\nu = -2$. As shown by the HF quasiparticle bands in Fig. 4(c), the two doped holes (marked by the black circle) are AFM aligned in valley/spin. The layer-resolved charge densities are shown in Fig. 4(d). Similar to the bilayer scenario, the interlayer excitons (dashed circles) in the upper (lower) moiré interface are antiparallel-spin aligned with the holes in the top (bottom) layer, while the two carrier holes (solid circles) are positioned individually in the top and bottom layers. Thus, a layered AFM order is established between the carriers in the two outer layers despite the lack of wave function overlap between the holes in two distinct layers.

To verify that the observed layered magnetic order is mediated by exciton, as shown in Fig. 4(e), we tune the exciton density n_x by decreasing the band gap E_g across the critical point. The phase indicator is defined as the energy difference between the layer-AFM state and layer-FM state, $\Delta E' = E_{LFM} - E_{LAFM}$. As presented

in Fig. 4(f), $\Delta E'$ vanishes simultaneously with n_X , i.e., without exciton, there is no magnetic order in the system. While we have chosen a special configuration of heterotrilinear moiré to present, this mechanism can establish layered magnetic order in more general configurations. The magnetic order between two outer layers will be determined not only by the exchange between carriers and excitons, but also by the interplay between excitons in the two moiré interfaces. In a general incommensurate trilayer system, the structure of this exchange requires more detailed study, which we leave for the future.

Conclusion and discussion. In this article, we have shown that exciton can help to establish and stabilize an effective ferromagnetic exchange between carriers widely separated in space. As such, externally injected exciton can be used to introduce long-range magnetic order in moiré superlattice. More practically, they may help to raise the Curie temperature in moiré superlattice, which is crucial, for example, for exploring the correlation phenomena that rely on magnetic order, such as the FQAH state. We limited our study to only a few set of parameters in this article. However, it is evident that the mechanism reported is universal in the large moiré family. While the calculations are performed for a ground state exciton-carrier mixture by tuning exciton density with a band gap parameter E_g much smaller than that in realistic compounds, the revealed mechanism of forming magnetic order through exciton-carrier exchange generally applies to systems with excitons injected either optically [22] or electrically [17]. We tune the gap parameters in Hartree-Fock calculation such that the Coulomb excitons have a density close to that of excitons injected by light in experiments [$O(0.1/\text{MUC})$].

The study presented in this article can be generalized immediately in a few aspects. For example, in trilayer moiré, we have chosen two outer layers to be aligned for simplicity, so there is only one moiré scale present in the problem. However, in realistic trilayer system, the two interfaces can have distinct moiré periodicity, leading to a bichromatic landscape for the Bose-Fermi mixture [39]. The consequence of the antiparallel-spin exchange between interlayer excitons and carriers in such complex

landscapes can be an interesting subject of study.

Acknowledgement. T. Tan acknowledges useful conversation with T. Devakul, J. Dong, A. P. Reddy, Yves Kwan. This work is supported by the National Key R&D Program of China (2020YFA0309600), Research Grant Council of Hong Kong SAR (AoE/P-701/20, HKU SRFS2122-7S05), and New Cornerstone Science Foundation. T. Tan is supported by Stanford Graduate Fellowship.

Appendix A: Hartree Fock Calculation

We performed Hartree-Fock calculation in plane-wave basis in TMD heterobilayer/trilayer. We detailed the operational perspective of the calculation in this appendix.

1. Single Particle Hamiltonian

The single-particle Hamiltonian of moiré TMD heterobilayer with Type-II band alignment for spin up (locked with $+K$ valley) is

$$H_{\uparrow} = \begin{pmatrix} \frac{(k-\kappa_-)^2}{2m_t} + V_t(\mathbf{r}) + E_g & T(\mathbf{r}) \\ T^{\dagger}(\mathbf{r}) & \frac{(k+\kappa_+)^2}{2m_b} + V_b(\mathbf{r}) \end{pmatrix}, \quad (\text{A1})$$

Its time reversal partner (spin down locked with $-K$ valley) is

$$H_{\downarrow} = \begin{pmatrix} \frac{(k+\kappa_-)^2}{2m_t} + V_t(\mathbf{r}) + E_g & T^{\dagger}(\mathbf{r}) \\ T(\mathbf{r}) & \frac{(k-\kappa_+)^2}{2m_b} + V_b(\mathbf{r}) \end{pmatrix}, \quad (\text{A2})$$

where $V_{t/b}(\mathbf{r}) = \sum_{i=1,3,5} 2V_{t/b} \cos(\mathbf{g}_i \cdot \mathbf{r} + \phi_{t/b})$, $T(\mathbf{r}) = w(1 + \omega e^{i\mathbf{g}_2 \cdot \mathbf{r}} + \omega^2 e^{i\mathbf{g}_3 \cdot \mathbf{r}})$, with $\mathbf{g}_i = b_M [\cos \frac{(i-1)\pi}{3}, \sin \frac{(i-1)\pi}{3}]$, b_M is the moiré reciprocal lattice constant, $\omega = e^{i\frac{2n\pi}{3}}$, where n is determined by angular momentum difference between orbitals involved.

For trilayer system, we take the single particle Hamiltonian to describe a sandwich-like structure, with outer two layers contributing valence band, and the middle layer contributing the conduction band. The single-particle Hamiltonians in the $+K$ and $-K$ valleys are

$$H_{\uparrow}^T = \begin{pmatrix} \frac{(k-\kappa_-)^2}{2m_t} + V_t(\mathbf{r}) & T(\mathbf{r}) & 0 \\ T^{\dagger}(\mathbf{r}) & \frac{(k-\kappa_+)^2}{2m_m} + V_m(\mathbf{r}) & T^{\dagger}(\mathbf{r}) \\ 0 & T(\mathbf{r}) & \frac{(k-\kappa_-)^2}{2m_b} + V_b(\mathbf{r}) \end{pmatrix} - E_g \begin{pmatrix} 1 & 0 & 0 \\ 0 & 0 & 0 \\ 0 & 0 & 1 \end{pmatrix}, \quad (\text{A3})$$

$$H_{\downarrow}^T = \begin{pmatrix} \frac{(k+\kappa_-)^2}{2m_t} + V_t(\mathbf{r}) & T^{\dagger}(\mathbf{r}) & 0 \\ T(\mathbf{r}) & \frac{(k+\kappa_+)^2}{2m_m} + V_m(\mathbf{r}) & T(\mathbf{r}) \\ 0 & T^{\dagger}(\mathbf{r}) & \frac{(k+\kappa_-)^2}{2m_b} + V_b(\mathbf{r}) \end{pmatrix} - E_g \begin{pmatrix} 1 & 0 & 0 \\ 0 & 0 & 0 \\ 0 & 0 & 1 \end{pmatrix}. \quad (\text{A4})$$

For Figs. 2 and 4, we set $w = 0$ to focus on the s-

wave channel exciton. When studying the nematic effect

[Fig. 3(a)], we set $w = 3$ meV.

2. Hartree-Fock Calculation

Let $c_{\mathbf{k},\mathbf{b},\tau,l}^\dagger$ be the electron creation operator in plane wave state with momentum $\mathbf{k} + \mathbf{b}$, measured relative to

γ point, \mathbf{b} is a moiré reciprocal lattice vector with basis \mathbf{g}_i , τ labels valley/spin (locked), l labels layer.

The many-body Hamiltonian is written as

$$\begin{aligned} \hat{H} = & \sum_{\substack{\mathbf{k} \in mBZ \\ \mathbf{b}_1, \mathbf{b}_2 \\ l_1, l_2, \tau}} T_{\mathbf{b}_1 l_1, \mathbf{b}_2 l_2}(\mathbf{k}, \tau) c_{\mathbf{k}, \mathbf{b}_1, l_1, \tau}^\dagger c_{\mathbf{k}, \mathbf{b}_2, l_2, \tau} \\ & + \frac{1}{2A} \sum_{\substack{\mathbf{k}_1 - \mathbf{k}_4 \in mBZ \\ \mathbf{b}_1 - \mathbf{b}_4 \\ l_1 l_2, \tau_1, \tau_2}} V_{l_1 l_2}(\mathbf{k}_1 + \mathbf{b}_1 - \mathbf{k}_3 - \mathbf{b}_3) \\ & \times c_{\mathbf{k}_1, \mathbf{b}_1, l_1, \tau_1}^\dagger c_{\mathbf{k}_2, \mathbf{b}_2, l_2, \tau_2}^\dagger c_{\mathbf{k}_4, \mathbf{b}_4, l_2, \tau_2} c_{\mathbf{k}_3, \mathbf{b}_3, l_1, \tau_1} \delta(\mathbf{k}_1 + \mathbf{b}_1 + \mathbf{k}_2 + \mathbf{b}_2 - \mathbf{k}_3 - \mathbf{b}_3 - \mathbf{k}_4 - \mathbf{b}_4), \end{aligned} \quad (\text{A5})$$

where $T_{\mathbf{b}_1 l_1, \mathbf{b}_2 l_2}(\mathbf{k}, \tau)$ is the matrix element of the single particle Hamiltonian H_τ (defined above) in the plane wave basis, A is sample area. $V(\mathbf{q})_{l_1, l_2}$ is the Fourier-transform of the Coulomb interaction between layer l_1

and l_2 , the delta function ensures momentum conservation. We take dual-gate screened Coulomb interaction and neglect inter-valley scattering.

$$V(\mathbf{q})_{l_1, l_2} = \frac{e^2}{2\epsilon_0 \epsilon_r |\mathbf{q}|} \left[\exp(-d|\mathbf{q}|) - \frac{2 \exp(-2D|\mathbf{q}|)}{1 + \exp(-2D|\mathbf{q}|)} \right], \quad (\text{A6})$$

d is vertical distance between layer l_1 and l_2 . We take inter-layer distance to be 0.7nm. D is the gate-to-sample

distance, we take $D = 10$ nm.

Hartree-Fock approximation consists of substituting the four-fermion operator by its pair-wise contraction

$$\begin{aligned} & c_{\mathbf{k}_1, \mathbf{b}_1, l_1, \tau_1}^\dagger c_{\mathbf{k}_2, \mathbf{b}_2, l_2, \tau_2}^\dagger c_{\mathbf{k}_4, \mathbf{b}_4, l_2, \tau_2} c_{\mathbf{k}_3, \mathbf{b}_3, l_1, \tau_1} \\ & \rightarrow c_{\mathbf{k}_1, \mathbf{b}_1, l_1, \tau_1}^\dagger c_{\mathbf{k}_3, \mathbf{b}_3, l_1, \tau_1} \langle c_{\mathbf{k}_2, \mathbf{b}_2, l_2, \tau_2}^\dagger c_{\mathbf{k}_4, \mathbf{b}_4, l_2, \tau_2} \rangle + \langle c_{\mathbf{k}_1, \mathbf{b}_1, l_1, \tau_1}^\dagger c_{\mathbf{k}_3, \mathbf{b}_3, l_1, \tau_1} \rangle c_{\mathbf{k}_2, \mathbf{b}_2, l_2, \tau_2}^\dagger c_{\mathbf{k}_4, \mathbf{b}_4, l_2, \tau_2} \\ & - \langle c_{\mathbf{k}_1, \mathbf{b}_1, l_1, \tau_1}^\dagger c_{\mathbf{k}_4, \mathbf{b}_4, l_2, \tau_2} \rangle c_{\mathbf{k}_2, \mathbf{b}_2, l_2, \tau_2}^\dagger c_{\mathbf{k}_3, \mathbf{b}_3, l_1, \tau_1} - c_{\mathbf{k}_1, \mathbf{b}_1, l_1, \tau_1}^\dagger c_{\mathbf{k}_4, \mathbf{b}_4, l_2, \tau_2} \langle c_{\mathbf{k}_2, \mathbf{b}_2, l_2, \tau_2}^\dagger c_{\mathbf{k}_3, \mathbf{b}_3, l_1, \tau_1} \rangle. \end{aligned} \quad (\text{A7})$$

The $\langle \rangle$ is taken with respect to the Slater determinant ground state constructed from the Hartree-Fock orbitals. We allow symmetry breaking at the moiré scale, and do

not allow inter-valley coherence.

$$\langle c_{\mathbf{k}_1, \mathbf{b}_1, l_1, \tau_1}^\dagger c_{\mathbf{k}_2, \mathbf{b}_2, l_2, \tau_2} \rangle \propto \delta_{\mathbf{k}_1, \mathbf{k}_2} \delta_{\tau_1, \tau_2}, \quad (\text{A8})$$

After this substitution, the Hartree-Fock Hamiltonian is

$$\begin{aligned}\hat{H}_H(\mathcal{P}) &= \sum_{\substack{\mathbf{k}_1, \mathbf{k}_2 \\ l_1, l_2, \tau_1, \tau_2 \\ \mathbf{b}_1 - \mathbf{b}_4}} c_{\mathbf{k}_1, \mathbf{b}_1, l_1, \tau_1}^\dagger c_{\mathbf{k}_1, \mathbf{b}_3, l_1, \tau_1} \mathcal{P}(\mathbf{k}_2, \tau_2)_{\mathbf{b}_4 l_2, \mathbf{b}_2 l_2} \frac{V_{l_1, l_2}(\mathbf{b}_1 - \mathbf{b}_3)}{A} \delta(\mathbf{b}_1 + \mathbf{b}_2 - \mathbf{b}_3 - \mathbf{b}_4) \\ &\equiv \sum_{\substack{\mathbf{k}_1 \\ l_1, \tau_1 \\ \mathbf{b}_1, \mathbf{b}_3}} c_{\mathbf{k}_1, \mathbf{b}_1, l_1, \tau_1}^\dagger [H_H(\mathbf{k}_1, \tau_1)_{\mathbf{b}_1 l_1, \mathbf{b}_3 l_1}] c_{\mathbf{k}_1, \mathbf{b}_3, l_1, \tau_1},\end{aligned}\tag{A9}$$

$$\begin{aligned}\hat{H}_F(\mathcal{P}) &= - \sum_{\substack{\mathbf{k}_1, \mathbf{k}_2 \\ l_1, l_2, \tau_1 \\ \mathbf{b}_1 - \mathbf{b}_4}} c_{\mathbf{k}_1, \mathbf{b}_1, l_1, \tau_1}^\dagger c_{\mathbf{k}_1, \mathbf{b}_4, l_2, \tau_1} \mathcal{P}(\mathbf{k}_2, \tau_1)_{\mathbf{b}_3 l_1, \mathbf{b}_2 l_2} \frac{V_{l_1, l_2}(\mathbf{k}_1 + \mathbf{b}_1 - \mathbf{k}_2 - \mathbf{b}_3)}{A} \delta(\mathbf{b}_1 + \mathbf{b}_2 - \mathbf{b}_3 - \mathbf{b}_4) \\ &\equiv \sum_{\substack{\mathbf{k}_1 \\ l_1, l_2, \tau_1 \\ \mathbf{b}_1, \mathbf{b}_4}} c_{\mathbf{k}_1, \mathbf{b}_1, l_1, \tau_1}^\dagger [H_F(\mathbf{k}_1, \tau_1)_{\mathbf{b}_1 l_1, \mathbf{b}_4 l_2}] c_{\mathbf{k}_1, \mathbf{b}_4, l_2, \tau_1},\end{aligned}\tag{A10}$$

$$\hat{H}_{HF} = \hat{H}_H(\mathcal{P} - \mathcal{P}_{CNP}) + \hat{H}_F(\mathcal{P} - \mathcal{P}_{CNP}) + \sum_{\substack{\mathbf{k} \in mBZ \\ \mathbf{b}_1, \mathbf{b}_2 \\ l_1, l_2, \tau}} T_{\mathbf{b}_1 l_1, \mathbf{b}_2 l_2}(\mathbf{k}, \tau) c_{\mathbf{k}, \mathbf{b}_1, l_1, \tau}^\dagger c_{\mathbf{k}, \mathbf{b}_2, l_2, \tau},\tag{A11}$$

where we have defined the projector \mathcal{P} as

$$\mathcal{P}(\mathbf{k}, \tau)_{\mathbf{b}_1 l_1, \mathbf{b}_2 l_2} \equiv \langle c_{\mathbf{k}, \mathbf{b}_2, l_2, \tau}^\dagger c_{\mathbf{k}, \mathbf{b}_1, l_1, \tau} \rangle.\tag{A12}$$

\mathcal{P}_{CNP} refers to projector evaluated with respect to the rotated isolated TMD hetero bilayer/trilayer filled to charge neutrality point (CNP), i.e., no interlayer tunneling $T(\mathbf{r})$ and moiré potential $V(\mathbf{r})$, only the kinetic term). This is to subtract off the charge background at charge neutrality [41].

The Hartree-Fock orbitals are eigenstates of \hat{H}_{HF}

$$d_{\mathbf{k}, n, \tau}^\dagger = \sum_{\mathbf{g}, l} z_{\mathbf{g}, l}^{n\mathbf{k}\tau} c_{\mathbf{k}, \mathbf{g}, l, \tau}^\dagger,\tag{A13}$$

where z is obtained by diagonalizing \hat{H}_{HF} in the c^\dagger, c basis, n labels the Hartree-Fock bands. The Slater de-

terminant ground state is

$$|\text{Slater}\rangle = \prod_{(n, \mathbf{k}, \tau) \in \text{filled}} d_{\mathbf{k}, n, \tau}^\dagger |\Omega\rangle.\tag{A14}$$

Then the projector is

$$\mathcal{P}(\mathbf{k}, \tau)_{\mathbf{b}_1 l_1, \mathbf{b}_2 l_2} = \sum_{n \in \text{filled}} z_{\mathbf{b}_1 l_1}^{n\mathbf{k}\tau} z_{\mathbf{b}_2 l_2}^{*n\mathbf{k}\tau}.\tag{A15}$$

Thus, H_{HF} and \mathcal{P} depends on each other: We need \mathcal{P} to construct the H_{HF} . We need eigenvectors of H_{HF} to construct \mathcal{P} . They are solved iteratively until convergence. The self-consistency condition is that the projector constructed from two iterative iteration are the same. We take the \mathbf{k} points to be

$$\mathbf{k} = \frac{n_1}{3} \mathbf{g}_1 + \frac{n_2}{3} \mathbf{g}_2,\tag{A16}$$

where $n_i = 0, 1, 2$. We keep all the $|\mathbf{b}| \leq 3|\mathbf{g}|$ in our calculation. Finally, notice that the total energy of the state is

$$E = \sum_{\mathbf{k}, \tau} Tr \left\{ \left[T(\mathbf{k}, \tau) + \frac{H_H(\mathbf{k}, \tau) + H_F(\mathbf{k}, \tau)}{2} \right] \times [\mathcal{P}(\mathbf{k}, \tau) - \mathcal{P}(\mathbf{k}, \tau)_{CNP}] \right\}.\tag{A17}$$

A initial guess for the projector is feed into the program for the first iteration. We use a variety of initial projector, including random seed and ansatz motivated by physical consideration, to locate the lowest-energy state.

3. Expanding the moiré unit cell

We mentioned in the main text that our Hartree-Fock calculation for the heterobilayer system is performed by

$$\hat{H}_d = \sum_{ij} \left[T_{ij} - \sum_{\gamma \in CNP} (V_{i\gamma j\gamma} - V_{i\gamma\gamma j}) \right] d_i^\dagger d_j + \frac{1}{2} \sum_{ijkl} V_{ijkl} d_i^\dagger d_j^\dagger d_l d_k. \quad (\text{A20})$$

To do exact diagonalization, we assume some orbitals to be frozen (filled background), while allowing a few orbitals to be active. The choice reflects the variational nature of exact diagonalization. In the case of our calculation, we allow the orbitals corresponding to the first

valence band of the two valleys to be active. We refer to the valence band that is not filled by an electron (doped hole) in the Hartree-Fock calculation as band 1, and the one that is filled by electron as band 2.

In this constrained Hilbert space, the many-body Hamiltonian is

$$\hat{H}_{d,proj} = \sum_{ij \in \text{active}} \left\{ T_{ij} + \sum_{k \in \text{frozen}} \left[V_{ikjk} - V_{ikkj} - \sum_{\gamma \in CNP} (V_{i\gamma j\gamma} - V_{i\gamma\gamma j}) \right] \right\} d_i^\dagger d_j^\dagger + \frac{1}{2} \sum_{ijkl \in \text{active}} V_{ijkl} d_i^\dagger d_j^\dagger d_l d_k. \quad (\text{A21})$$

Other terms that take us out of the constrained Hilbert space are left away. If the frozen orbitals we choose are

the same as those filled orbitals in the Hartree-Fock calculation (frozen=occ), then we can replace

$$T_{ij} + \sum_{k \in \text{frozen}} (V_{ikjk} - V_{ikkj}) - \sum_{\gamma \in CNP} (V_{i\gamma j\gamma} - V_{i\gamma\gamma j}) \rightarrow \epsilon_i \delta_{ij}. \quad (\text{A22})$$

In this case, we can treat the Hartree-Fock orbital energy as if it is the single-particle energy associated with that orbital. However, in the more general case where the

frozen subspace and the filled orbitals in Hartree-Fock calculation are different, e.g., when the frozen subspace is a subset of the later, then

$$\hat{H}_{d,proj} = \sum_{ij \in \text{active}} \left[\epsilon_i \delta_{ij} - \sum_{k \in \text{occ-frozen}} (V_{ikjk} - V_{ikkj}) \right] d_i^\dagger d_j^\dagger + \frac{1}{2} \sum_{ijkl \in \text{active}} V_{ijkl} d_i^\dagger d_j^\dagger d_l d_k. \quad (\text{A23})$$

Our calculation is this latter case, since we dope one hole in our Hartree-Fock calculation. Then *occ-frozen* refers to the valence band that is previously filled in the

Hartree-Fock calculation, but now chosen as the active subspace. The magnon gap is defined as flipping the spin/valley of one electron, i.e.,

$$\Delta_{mag}(n_X) = E(N_1 = 1, N_2 = N_{\max} - 1, n_X) - E(N_1 = 0, N_2 = N_{\max}, n_X) - [E(N_1 = 1, N_2 = N_{\max} - 1, 0) - E(N_1 = 0, N_2 = N_{\max}, 0)], \quad (\text{A24})$$

where N_i is the particle number in band i . For a finite-size study with $N \times N$ momentum grid, $N_{\max} = N^2$. n_X is the exciton density, controlled by the band gap E_g . We subtract off the background contribution at $n_X = 0$ since we are flipping electrons in the momentum space rather than real space, there are Fock energy changes associated

with the flipping process. This does not contribute to the long-range magnetic order.

Appendix B: Wave Packet Calculation

Here we derive the interaction between a carrier and an exciton. For the sake of concreteness, we take the carrier to be an electron, although taking the carrier to be hole does not change the resulting expression of the exchange interaction.

The starting point of our analysis is the following Hamiltonian, which is just the standard second-quantized Hamiltonian including Coulomb interaction

$$H = \sum_i \epsilon c_i^\dagger c_i + \frac{1}{2} \sum_{i,j,k,l} \langle ij|V_c|lk\rangle c_i^\dagger c_j^\dagger c_k c_l - \sum_{i,j} \langle i|V_{single}|j\rangle c_i^\dagger c_j. \quad (\text{B1})$$

In the absence of the Coulomb interaction, the ground state is simply the state with lowest N electron levels occupied. We are concerned with the effect of Coulomb interaction on spin alignment, thus we can safely ignore the kinetic and single-particle potential terms. Additionally, we call the states above the Fermi level "electron states" and states below the "hole states". The creation/annihilation operator of the hole states is the annihilation/creation operator of the electron states ($h_i^\dagger = e_i$). With all these, the Hamiltonian for Coulomb interaction can be separated into three groups, i.e., between

electrons, between holes, between electrons and holes.

$$H_{ee} = \frac{1}{2} \sum_{i,j,k,l} \langle ij|V|kl\rangle e_i^\dagger e_j^\dagger e_l e_k, \quad (\text{B2})$$

$$H_{hh} = \frac{1}{2} \sum_{\alpha,\beta,\gamma,\delta} \langle \alpha\beta|V|\gamma\delta\rangle h_\delta^\dagger h_\gamma^\dagger h_\alpha h_\beta, \quad (\text{B3})$$

$$H_{eh} = \sum_{i,j,\alpha,\beta} [\langle i\beta|V|\alpha j\rangle - \langle i\beta|V|j\alpha\rangle] e_i^\dagger h_\alpha^\dagger h_\beta e_j. \quad (\text{B4})$$

Notice that we have retained only those terms that preserve hole numbers as well as electron numbers. This is because we will be taking matrix elements of the Hamiltonian between states that preserve these quantities. Additionally, when producing H_{eh} , we have discarded those δ terms arising from the commutation relations, as they only contribute to the kinetic terms. For convenience, we will discuss the scenario where the doped carrier is electron. But the discussion where the doped carrier is hole is completely analogous.

If we take matrix elements of the Hamiltonian between states consisting of one exciton and one electron (e.g. one electron plus one exciton). The following terms will be produced, where $|FS\rangle$ is the Fermi sea state and labels such as h and $e'1$ are compound indices that includes the momentum and spin/valley,

$$\begin{aligned} & \langle c_{e'1} c_{e'2} v_{h'} | H_{ee} | c_{e1} c_{e2} v_h \rangle \\ &= \frac{1}{2} \sum_{ijkl} V_{ijkl} \delta_{h,h'} \langle FS | e_{e'2} e_{e'1} e_i^\dagger e_j^\dagger e_l e_k e_{e1}^\dagger e_{e2}^\dagger | FS \rangle \\ &= \frac{1}{2} \sum_{ijkl} V_{ijkl} \delta_{h,h'} (\delta_{e'1,i} \delta_{j,e'2} - \delta_{e'1,j} \delta_{i,e'2}) (\delta_{l,e2} \delta_{k,e1} - \delta_{k,e2} \delta_{l,e1}) \\ &= \delta_{hh'} (V_{e'1e'2,e1e2} - V_{e'1e'2,e2e1}) \\ &\sim -\delta_{hh'} V_{e'1e'2,e2e1}, \end{aligned} \quad (\text{B5})$$

$$\begin{aligned} & \langle c_{e'1} c_{e'2} v_{h'} | H_{eh} | c_{e1} c_{e2} v_h \rangle \\ &= \sum_{i,j,\alpha,\beta} (V_{i\beta,\alpha j} - V_{i\beta,j\alpha}) \delta_{\beta h} \delta_{h'\alpha} (\delta_{e'2e2} \delta_{i,e'1} \delta_{j,e1} - \delta_{e'2,e1} \delta_{i,e'1} \delta_{j,e2} - \delta_{i,e'2} \delta_{j,e1} \delta_{e'1,e2} + \delta_{e2,j} \delta_{e'1e1} \delta_{i,e'2}) \\ &= (V_{e'1h,h'e1} - V_{e'1h,e1h'}) \delta_{e'2e2} - (V_{e'1h,h'e2} - V_{e'1h,e2h'}) \delta_{e'2e1} \\ &\quad - (V_{e'2h,h'e1} - V_{e'2h,e1h'}) \delta_{e'1e2} + (V_{e'2h,h'e2} - V_{e'2h,e2h'}) \delta_{e'1e1} \\ &\sim V_{e'1h,e2h'} \delta_{e'2e1} + V_{e'2h,e1h'} \delta_{e'1e2}. \end{aligned} \quad (\text{B6})$$

Notice that we have used in our derivation the fact that

(since V only depends on the magnitude of its argument)

$$V_{e'1e'2,e1e2} = \int dr_1 dr_2 \psi_{e'1}^*(r_1) \psi_{e'2}^*(r_2) V(r_1 - r_2) \psi_{e1}^*(r_1) \psi_{e2}^*(r_2) = V_{e'2e'1,e2e1}. \quad (\text{B7})$$

And the \sim means omitting direct terms (e.g., $\delta_{hh'}V_{e'1e'2,e1e2}$) and terms that involve the overlapping of wave function on two different layers (e.g., $\delta_{e'2e2}V_{e'1h,h'e1}$).

This is a good place to clarify a tricky notation prob-

lem: it should also be noticed that when we compute the matrix elements of the Coulomb interaction, we are doing it with respect to the vacuum state rather than the Fermi sea state. Assume $(h'1, h'2, h1, h2)$ are hole labels.

$$V_{h'1h'2,h1h2} = \int dr_1 dr_2 \psi_{h'_1}^*(r_1) \psi_{h'_2}^*(r_2) V(r_1 - r_2) \psi_{h_1}(r_1) \psi_{h_2}(r_2). \quad (\text{B8})$$

In the plane wave basis, the Coulomb matrix elements

have the following form, where k_i is momentum labels are σ_i are spin/valley labels.

$$\begin{aligned} V_{k_1 k_2, k_3 k_4} &= \frac{1}{A^2} \int dr_1 dr_2 e^{-ik_1 r_1} e^{-ik_2 r_2} e^{ik_3 r_1} e^{ik_4 r_2} V(r_1 - r_2) \delta_{\sigma_1, \sigma_3} \delta_{\sigma_2, \sigma_4} \\ &= \int d(r_1 - r_2) dr_2 V(r_1 - r_2) e^{i(k_3 - k_1)(r_1 - r_2)} e^{i(k_4 - k_2 + k_3 - k_1)r_2} \delta_{\sigma_1, \sigma_3} \delta_{\sigma_2, \sigma_4} \\ &= \frac{V_{l_1 l_2}(k_3 - k_1)}{A} \delta_{k_1 + k_2, k_3 + k_4} \delta_{\sigma_1, \sigma_3} \delta_{\sigma_2, \sigma_4}, \end{aligned} \quad (\text{B9})$$

where A is the system area, $V_{l_i l_j}(k)$ is the Fourier transform of Coulomb interaction between layer i and j .

The moiré trapped electron state has the following expression

$$c_{j,\sigma}^\dagger |FS\rangle = \sum_{k_e} e^{-ik_e R_j} W_e(k_e) e_{k_e,\sigma}^\dagger |FS\rangle. \quad (\text{B10})$$

We require the electron to be trapped (up to normaliza-

tion)

$$\begin{aligned} \sum_{k_e} W_e(k_e) e^{ik_e(R_e - R_j)} &\propto e^{-(R_j - R_e)^2 / a_e^2} \\ \Rightarrow W_e(k_e) &= \frac{a_e^2}{2} e^{-\frac{1}{4} a_e^2 k_e^2}. \end{aligned} \quad (\text{B11})$$

The trapped exciton state has the following expression, where $a_{k,\sigma_e\sigma_h}^\dagger$ creates an exciton of COM momentum k . q_x is basically the relative momentum between an electron and a hole.

$$\begin{aligned} &a_{j,\sigma_e,\sigma_h}^\dagger |FS\rangle \\ &= \sum_k e^{-ikR_j} W_x(k) a_{k,\sigma_e\sigma_h}^\dagger |FS\rangle \\ &= \sum_{k,q_x} e^{-ikR_j} W_x(k) \psi_x(q_x) e_{q_x + \frac{m_e}{M}k, \sigma_e}^\dagger h_{q_x - \frac{m_h}{M}k, \sigma_h}^\dagger |FS\rangle \\ &= \int \sum_{k,q_x} W_x(k) e^{-ikR_j} dR_e dR_h \psi_x(q_x) e^{i(q_x + \frac{m_e}{M}k)R_e} e^{-i(q_x - \frac{m_h}{M}k)R_h} e_{R_e, \sigma_e}^\dagger h_{R_h, \sigma_h}^\dagger |FS\rangle \\ &\propto \int \sum_{k,q_x} e^{-ikR_j} W_x(k) dR_c dR_r \psi_x(q_x) e^{iq_x R_r} e^{ikR_c} e_{R_e(R_c, R_r), \sigma_e}^\dagger h_{R_h(R_c, R_r), \sigma_h}^\dagger |FS\rangle. \end{aligned} \quad (\text{B12})$$

We require the exciton to be trapped (up to normalization)

$$\begin{aligned} \sum_k e^{ik(R_c - R_j)} W_x(k) &\propto e^{-(R_c - R_j)^2 / a_x^2} \\ \Rightarrow W_x(k) &= \frac{a_x^2}{2} e^{-\frac{1}{4} a_x^2 k^2}. \end{aligned} \quad (\text{B13})$$

We also require, owing to the exciton being in $1s$ state, that

$$\begin{aligned} \sum_{q_x} e^{iq_x R_r} \psi_x(q_x) &\propto e^{-R_r/a_b} \\ \Rightarrow \psi_x(q_x) &= \frac{a_b^2}{(1 + a_b^2 q_x^2)^{\frac{3}{2}}}. \end{aligned} \quad (\text{B14})$$

We then evaluated the matrix elements in the following basis state (doped electron trapped at R_i and exciton trapped at R_j)

$$\begin{aligned} &|\Psi_{ij,\sigma\sigma_e\sigma_h}\rangle \\ &= c_{i,\sigma}^\dagger a_{j,\sigma_e\sigma_h}^\dagger |FS\rangle \\ &= C \sum_{k,q_x,k_e} e^{-ik_e R_i} W_e(k_e) e^{-ik R_j} W_x(k) \end{aligned} \quad (\text{B15}) \quad \text{in which the expressions}$$

$$\times \psi_x(q_x) e_{k_e,\sigma}^\dagger e_{q_x + \frac{m_e}{M} k, \sigma_e}^\dagger e_{q_x - \frac{m_h}{M} k, \sigma_h}^\dagger |FS\rangle,$$

$$\frac{1}{C_0^2} = \frac{A^3}{(2\pi)^6} \frac{\pi^3 a_x^2 a_e^2 a_b^2}{8}, \quad (\text{B17})$$

$$\begin{aligned} c_1 &= \frac{A^3}{(2\pi)^6} \int dk dq_x dk_e e^{i(q_x + \frac{m_e}{M} k - k_e)(R_i - R_j)} W_e(k_e) W_e(q_x + \frac{m_e}{M} k) W_x(k) W_x(k_e - q_x + \frac{m_h}{M} k) \\ &\times \psi_x(q_x) \psi_x\left(\frac{m_e}{M} q_x + \frac{m_h}{M} k_e - \frac{\mu}{M} k\right). \end{aligned} \quad (\text{B18})$$

Defining $\frac{1}{C_1^2} = \frac{1}{C_0^2} - c_1$, the three terms we need to cal-

culate are

$$\begin{aligned} &\langle \Psi_{ij,\sigma'\sigma'_e\sigma'_h} | H_{ee} | \Psi_{ij,\sigma\sigma_e\sigma_h} \rangle \\ &\supseteq -\frac{C_1^2}{A} \sum_{k,q_x,k_e,k',q'_x,k'_e} e^{-i(k_e - k'_e)R_i} e^{-i(k - k')R_j} \psi_x(q_x) \psi_x^*(q'_x) W_e(k_e) W_e^*(k'_e) W_x(k) W_x^*(k') \\ &\quad \times \delta_{\sigma_h,\sigma'_h} \delta_{\sigma_e,\sigma'_e} \delta_{\sigma,\sigma'_e} \delta_{q_x - \frac{m_h}{M} k, q'_x - \frac{m_h}{M} k'} \delta_{k_e + q_x + \frac{m_e}{M} k, k'_e + q'_x + \frac{m_e}{M} k'} V_{ee}(q_x + \frac{m_e}{M} k - k'_e) \\ &= -\frac{C_1^2}{A} \sum_{k,q_x,k_e,k'} e^{i(k - k')(R_i - R_j)} \psi_x(q_x) \psi_x^*(q_x - \frac{m_h}{M} (k - k')) W_e(k_e) W_e^*(k_e + k - k') W_x(k) W_x^*(k') \\ &\quad \times \delta_{\sigma_h,\sigma'_h} \delta_{\sigma_e,\sigma'_e} \delta_{\sigma,\sigma'_e} V_{ee}(q_x + \frac{m_e}{M} k - k_e - k + k') \\ &\equiv I_{ee}, \end{aligned} \quad (\text{B19})$$

$$\begin{aligned} &\langle \Psi_{ij,\sigma'\sigma'_e\sigma'_h} | H_{eh} | \Psi_{ij,\sigma\sigma_e\sigma_h} \rangle \\ &\supseteq \frac{C_1^2}{A} \sum_{k,q_x,k_e,k',q'_x,k'_e} e^{-i(k_e - k'_e)R_i} e^{-i(k - k')R_j} \psi_x(q_x) \psi_x^*(q'_x) W_e(k_e) W_e^*(k'_e) W_x(k) W_x^*(k') \\ &\quad \times \delta_{\sigma',\sigma_e} \delta_{k'_e, q_x + \frac{m_e}{M} k} \delta_{\sigma'_e,\sigma} \delta_{\sigma_h,\sigma'_h} \delta_{q'_x + \frac{m_e}{M} k' + q_x - \frac{m_h}{M} k, k_e + q'_x - \frac{m_h}{M} k'} V_{eh}(q'_x + \frac{m_e}{M} k' - k_e) \\ &= \frac{C_1^2}{A} \sum_{k,q'_x,k'_e,k'} e^{i(k - k')(R_i - R_j)} \psi_x(k'_e - \frac{m_e}{M} k) \psi_x^*(q'_x) W_e(k'_e + k' - k) W_e^*(k'_e) W_x(k) W_x^*(k') \\ &\quad \times \delta_{\sigma',\sigma_e} \delta_{\sigma'_e,\sigma} \delta_{\sigma_h,\sigma'_h} V_{eh}(q'_x + \frac{m_e}{M} k' - k' - k'_e + k), \end{aligned} \quad (\text{B20})$$

$$\begin{aligned}
& \langle \Psi_{ij,\sigma'\sigma'_e\sigma'_h} | H_{eh} | \Psi_{ij,\sigma\sigma_e\sigma_h} \rangle \\
& \supseteq \frac{C_1^2}{A} \sum_{k,q_x,k_e,k',q'_x,k'_e} e^{-i(k_e-k'_e)R_i} e^{-i(k-k')R_j} \psi_x(q_x) \psi^*(q'_x) W_e(k_e) W_e^*(k'_e) W_x(k) W_x^*(k') \\
& \quad \times \delta_{\sigma,\sigma'_e} \delta_{k_e,q'_x+\frac{m_e k'}{M}} \delta_{\sigma_e,\sigma'} \delta_{\sigma_h,\sigma'_h} \delta_{k'_e+q_x-\frac{m_h k}{M}} \delta_{k,q_x+\frac{m_e k+q'_x}{M}} \delta_{k',q'_x-\frac{m_h k'}{M}} V_{eh}(-q_x - \frac{m_e k + k'_e}{M}) \\
& = \frac{C_1^2}{A} \sum_{k,q_x,k_e,k'} e^{i(k-k')(R_i-R_j)} \psi_x(q_x) \psi^*(k_e - \frac{m_e k'}{M}) W_e(k_e) W_e^*(k_e + k - k') W_x(k) W_x^*(k') \\
& \quad \times \delta_{\sigma,\sigma'_e} \delta_{\sigma_e,\sigma'} \delta_{\sigma_h,\sigma'_h} V_{eh}(-q_x - \frac{m_e k + k_e + k - k'}{M}) \\
& \equiv I_{eh}.
\end{aligned} \tag{B21}$$

Notice that under the mild assumption that W 's and ψ 's are all real, then the last two terms are complex conjugate of each other. If we further assume that W 's and ψ 's are

even, then the last two terms are both real. It's also trivial to prove that the term from H_{ee} is real. Thus the effective Hamiltonian takes the following form:

$$H_{eff} = \sum_{ij,\sigma,\sigma_e,\sigma_h} (I_{ee} + 2I_{eh}) c_{i,\sigma}^\dagger a_{j,\sigma_e,\sigma_h}^\dagger a_{j,\sigma,\sigma_h} c_{i,\sigma_e} \equiv \sum_{ij,\sigma,\sigma_e,\sigma_h} J c_{i,\sigma}^\dagger a_{j,\sigma_e,\sigma_h}^\dagger a_{j,\sigma,\sigma_h} c_{i,\sigma_e}. \tag{B22}$$

We have used C_1^2 rather than C^2 when calculating the matrix elements. This is because by using C_1^2 rather than

C^2 , we have discarded the following term in the effective Hamiltonian

$$\begin{aligned}
H_{dis} & \propto \sum_{\sigma,\sigma_h,i,j} c_{i,\sigma}^\dagger a_{j,-\sigma,\sigma_h}^\dagger a_{j,\sigma,\sigma_h} c_{i,-\sigma} \\
& = \sum_{\sigma,\sigma_h,i,j} c_{i,\sigma}^\dagger c_{i,-\sigma} c_{j,-\sigma}^\dagger c_{j,\sigma} v_{j,\sigma_h}^\dagger v_{j,\sigma_h} - c_{i,\sigma}^\dagger c_{i,\sigma} v_{i,\sigma_h}^\dagger v_{i,\sigma_h} \delta_{ij} \\
& = \sum_{i,j} N_j^{hole} (S_i^+ S_j^- + S_i^- S_j^+) - \sum_i N_i^{electron} N_i^{hole},
\end{aligned} \tag{B23}$$

N_i counts the particle number at R_i . We have used the usual substitution between spin operators and electron

creation/annihilation operators

$$\begin{aligned}
S^+ & = e_\uparrow^\dagger e_\downarrow, \\
S^- & = e_\downarrow^\dagger e_\uparrow, \\
S^z & = \frac{1}{2} (e_\uparrow^\dagger e_\uparrow - e_\downarrow^\dagger e_\downarrow).
\end{aligned} \tag{B24}$$

Now it's easy to see that the first term in H_{dis} is an in-plane term and it does not contribute to the magnetic order. The second term counts the particle number, and it also does not contribute to the magnetic order.

- ture **556**, 43 (2018).
- [2] E. Y. Andrei and A. H. MacDonald, Graphene bilayers with a twist, *Nat. Mater.* **19**, 1265–1275 (2020).
 - [3] L. Balents, C. R. Dean, D. K. Efetov, and A. F. Young, Superconductivity and strong correlations in moiré flat bands, *Nat. Phys.* **16**, 725 (2020).
 - [4] D. M. Kennes, M. Claassen, L. Xian, A. Georges, A. J. Millis, J. Hone, C. R. Dean, D. N. Basov, A. N. Pasupathy, and A. Rubio, Moiré heterostructures as a condensed-matter quantum simulator, *Nat. Phys.* **17**, 155–163 (2021).
 - [5] E. Y. Andrei, D. K. Efetov, P. Jarillo-Herrero, A. H. MacDonald, K. F. Mak, T. Senthil, E. Tutuc, A. Yazdani, and A. F. Young, The marvels of moiré materials, *Nat. Rev. Mater.* **6**, 201 (2021).
 - [6] N. P. Wilson, W. Yao, J. Shan, and X. Xu, Excitons and emergent quantum phenomena in stacked 2d semiconductors, *Nature* **599**, 383 (2021).
 - [7] E. C. Regan, D. Wang, E. Y. Paik, Y. Zeng, L. Zhang, J. Zhu, A. H. MacDonald, H. Deng, and F. Wang, Emerging exciton physics in transition metal dichalcogenide heterobilayers, *Nat. Rev. Mater.* **7**, 778 (2022).
 - [8] C. N. Lau, M. W. Bockrath, K. F. Mak, and F. Zhang, Reproducibility in the fabrication and physics of moiré materials, *Nature* **602**, 41 (2022).
 - [9] D. Huang, J. Choi, C.-K. Shih, and X. Li, Excitons in semiconductor moiré superlattices, *Nat. Nanotechnol.* **17**, 227 (2022).
 - [10] H. Yu, G.-B. Liu, J. Tang, X. Xu, and W. Yao, Moiré excitons: From programmable quantum emitter arrays to spin-orbit-coupled artificial lattices, *Sci. Adv.* **3**, e1701696 (2017).
 - [11] K. L. Seyler, P. Rivera, H. Yu, N. P. Wilson, E. L. Ray, D. G. Mandrus, J. Yan, W. Yao, and X. Xu, Signatures of moiré-trapped valley excitons in $\text{MoSe}_2/\text{WSe}_2$ heterobilayers, *Nature* **567**, 66 (2019).
 - [12] C. Jin, E. C. Regan, A. Yan, M. Iqbal Bakti Utama, D. Wang, S. Zhao, Y. Qin, S. Yang, Z. Zheng, S. Shi, *et al.*, Observation of moiré excitons in WSe_2/WS_2 heterostructure superlattices, *Nature* **567**, 76 (2019).
 - [13] K. Tran, G. Moody, F. Wu, X. Lu, J. Choi, K. Kim, A. Rai, D. A. Sanchez, J. Quan, A. Singh, *et al.*, Evidence for moiré excitons in van der waals heterostructures, *Nature* **567**, 71 (2019).
 - [14] E. M. Alexeev, D. A. Ruiz-Tijerina, M. Danovich, M. J. Hamer, D. J. Terry, P. K. Nayak, S. Ahn, S. Pak, J. Lee, J. I. Sohn, *et al.*, Resonantly hybridized excitons in moiré superlattices in van der waals heterostructures, *Nature* **567**, 81 (2019).
 - [15] M. Brotons-Gisbert, H. Baek, A. Molina-Sánchez, A. Campbell, E. Scerri, D. White, K. Watanabe, T. Taniguchi, C. Bonato, and B. D. Gerardot, Spin-layer locking of interlayer excitons trapped in moiré potentials, *Nat. Mater.* **19**, 630 (2020).
 - [16] P. Rivera, H. Yu, K. L. Seyler, N. P. Wilson, W. Yao, and X. Xu, Interlayer valley excitons in heterobilayers of transition metal dichalcogenides, *Nat. Nanotechnol.* **13**, 1004 (2018).
 - [17] Z. Wang, D. A. Rhodes, K. Watanabe, T. Taniguchi, J. C. Hone, J. Shan, and K. F. Mak, Evidence of high-temperature exciton condensation in two-dimensional atomic double layers, *Nature* **574**, 76 (2019).
 - [18] W. Li, X. Lu, S. Dubey, L. Devenica, and A. Srivastava, Dipolar interactions between localized interlayer excitons in van der waals heterostructures, *Nat. Mater.* **19**, 624 (2020).
 - [19] H. Park, J. Zhu, X. Wang, Y. Wang, W. Holtzmann, T. Taniguchi, K. Watanabe, J. Yan, L. Fu, T. Cao, *et al.*, Dipole ladders with large Hubbard interaction in a moiré exciton lattice, *Nat. Phys.* **19**, 1286 (2023).
 - [20] Z. Lian, Y. Meng, L. Ma, I. Maity, L. Yan, Q. Wu, X. Huang, D. Chen, X. Chen, X. Chen, *et al.*, Valley-polarized excitonic mott insulator in WS_2/WSe_2 moiré superlattice, *Nat. Phys.* **20**, 34 (2024).
 - [21] R. Xiong, J. H. Nie, S. L. Brantly, P. Hays, R. Sailus, K. Watanabe, T. Taniguchi, S. Tongay, and C. Jin, Correlated insulator of excitons in WSe_2/WS_2 moiré superlattices, *Science* **380**, 860 (2023).
 - [22] X. Wang, C. Xiao, H. Park, J. Zhu, C. Wang, T. Taniguchi, K. Watanabe, J. Yan, D. Xiao, D. R. Gamelin, *et al.*, Light-induced ferromagnetism in moiré superlattices, *Nature* **604**, 468 (2022).
 - [23] X. Wang, X. Zhang, J. Zhu, H. Park, Y. Wang, C. Wang, W. G. Holtzmann, T. Taniguchi, K. Watanabe, J. Yan, D. R. Gamelin, W. Yao, D. Xiao, T. Cao, and X. Xu, Intercell moiré exciton complexes in electron lattices, *Nat. Mater.* **22**, 599–604 (2023).
 - [24] B. Gao, D. G. Suárez-Forero, S. Sarkar, T.-S. Huang, D. Session, M. J. Mehrabad, R. Ni, M. Xie, P. Upadhyay, J. Vannucci, *et al.*, Excitonic Mott insulator in a Bose-Fermi-Hubbard system of moiré WS_2/WSe_2 heterobilayer, *Nat. Commun.* **15**, 2305 (2024).
 - [25] Y. Tang, L. Li, T. Li, Y. Xu, S. Liu, K. Barkmak, K. Watanabe, T. Taniguchi, A. H. MacDonald, J. Shan, *et al.*, Simulation of hubbard model physics in WSe_2/WS_2 moiré superlattices, *Nature* **579**, 353 (2020).
 - [26] E. Anderson, F.-R. Fan, J. Cai, W. Holtzmann, T. Taniguchi, K. Watanabe, D. Xiao, W. Yao, and X. Xu, Programming correlated magnetic states with gate-controlled moiré geometry, *Science* **381**, 325–330 (2023).
 - [27] J. Cai, E. Anderson, C. Wang, X. Zhang, X. Liu, W. Holtzmann, Y. Zhang, T. Fan, Fengren and d Taniguchi, K. Watanabe, Y. Ran, T. Cao, L. Fu, D. Xiao, W. Yao, and X. Xu, Signatures of fractional quantum anomalous Hall states in twisted MoTe_2 , *Nature* **622**, 63 (2023).
 - [28] H. Park, J. Cai, E. Anderson, Y. Zhang, J. Zhu, X. Liu, C. Wang, W. Holtzmann, C. Hu, Z. Liu, T. Taniguchi, K. Watanabe, J.-H. Chu, T. Cao, L. Fu, W. Yao, C.-Z. Chang, D. Cobden, D. Xiao, and X. Xu, Observation of fractionally quantized anomalous Hall effect, *Nature* **622**, 74 (2023).
 - [29] Y. Zeng, Z. Xia, K. Kang, J. Zhu, P. Knüppel, C. Vaswani, K. Watanabe, T. Taniguchi, K. F. Mak, and J. Shan, Thermodynamic evidence of fractional chern insulator in moiré MoTe_2 , *Nature* **622**, 69 (2023).
 - [30] F. Xu, Z. Sun, T. Jia, C. Liu, C. Xu, C. Li, Y. Gu, K. Watanabe, T. Taniguchi, B. Tong, *et al.*, Observation of integer and fractional quantum anomalous hall effects in twisted bilayer MoTe_2 , *Phys. Rev. X* **13**, 031037 (2023).
 - [31] M. Serlin, C. Tschirhart, H. Polshyn, Y. Zhang, J. Zhu, K. Watanabe, T. Taniguchi, L. Balents, and A. Young, Intrinsic quantized anomalous hall effect in a moiré heterostructure, *Science* **367**, 900 (2020).
 - [32] T. Li, S. Jiang, B. Shen, Y. Zhang, L. Li, Z. Tao, T. Devakul, K. Watanabe, T. Taniguchi, L. Fu, *et al.*, Quan-

- tum anomalous hall effect from intertwined moiré bands, *Nature* **600**, 641 (2021).
- [33] A. P. Reddy, F. Alsallom, Y. Zhang, T. Devakul, and L. Fu, Fractional quantum anomalous hall states in twisted bilayer MoTe_2 and WSe_2 , *Phys. Rev. B* **108**, 085117 (2023).
- [34] C. Xiao, Y. Wang, and W. Yao, Dynamic generation of spin spirals of moiré trapped carriers via exciton mediated spin interactions, *Nano Lett.* **23**, 1872 (2023).
- [35] M. H. Naik, E. C. Regan, Z. Zhang, Y.-H. Chan, Z. Li, D. Wang, Y. Yoon, C. S. Ong, W. Zhao, S. Zhao, *et al.*, Intralayer charge-transfer moiré excitons in van der waals superlattices, *Nature* **609**, 52 (2022).
- [36] F. Wu, T. Lovorn, E. Tutuc, and A. H. MacDonald, Hubbard model physics in transition metal dichalcogenide moiré bands, *Phys. Rev. Lett.* **121**, 026402 (2018).
- [37] Q. Zhu, M. W.-Y. Tu, Q. Tong, and W. Yao, Gate tuning from exciton superfluid to quantum anomalous hall in van der waals heterobilayer, *Sci. Adv.* **5**, eaau6120 (2019).
- [38] Q. Tong, H. Yu, Q. Zhu, Y. Wang, X. Xu, and W. Yao, Topological mosaics in moiré superlattices of van der waals heterobilayers, *Nature Phys.* **13**, 356 (2017).
- [39] Q. Tong, M. Chen, F. Xiao, H. Yu, and W. Yao, Interferences of electrostatic moiré potentials and bichromatic superlattices of electrons and excitons in transition metal dichalcogenides, *2D Mater.* **8**, 025007 (2020).
- [40] T.-S. Huang, P. Lunts, and M. Hafezi, Nonbosonic moiré excitons, *Phys. Rev. Lett.* **132**, 186202 (2024).
- [41] M. Xie and A. H. MacDonald, Nature of the correlated insulator states in twisted bilayer graphene, *Phys. Rev. Lett.* **124**, 097601 (2020).
- [42] G. Giuliani and G. Vignale, The Hartree–Fock approximation, in *Quantum Theory of the Electron Liquid* (Cambridge University Press, 2005) p. 69–110.